Common Self-polar Triangle of Concentric Conics for Light Field Camera Calibration

Qi Zhang and Qing Wang(✉)

School of Computer Science, Northwestern Polytechnical University, Xi'an 710072, China
qwang@nwpu.edu.cn

Abstract. Accurate light field camera calibration plays an important role in various applications. Instead of a planar checkerboard, we propose to calibrate light field camera using a concentric conics pattern. In this paper, we explore the property and reconstruction of common self-polar triangle with respect to concentric circle and ellipse. A light field projection model is formulated to compute out an effective linear initial solution for both intrinsic and extrinsic parameters. In addition, a 4-parameter radial distortion model is presented considering different view points in light field. Finally, we establish a cost function based on Sampson error for non-linear optimization. Experimental results on both synthetic data and real light field have verified the effectiveness and robustness of the proposed algorithm.

Keywords: Computational photography and video · Light field camera calibration · Common self-polar triangle

1 Introduction

Light field camera [23] captures spatial and angular information of light rays in the space, which provides multi-view observations of a scene with a single shot. Sophisticated post-processing techniques [14,22,27,31–33,38,39] ranging from digital refocusing to depth estimation have been introduced in decades. It is a crucial step to calibrate light field camera in various applications, such as registration [16], 3D reconstruction [36,37], light field stitching [1,9,26] and visual metrology [5,7].

In general, there are three popular types of meta-patterns for camera calibration, which are points, lines and conics. Existing approaches [2,3,6,15,29,30,34,35] usually utilize checkerboard to detect corner points or line features for light field camera calibration. However, several open issues still remain. Firstly, it is difficult to extract accurate locations of corner points due to the effect of noise and the quality of sub-aperture image. Secondly, considering the fact that the line feature [2] is detected from micro-lens images in light field raw data

Supported by NSFC under Grant 61531014.

C. V. Jawahar et al. (Eds.): ACCV 2018, LNCS 11366, pp. 18–33, 2019.
https://doi.org/10.1007/978-3-030-20876-9_2

directly, the low resolution of micro-lens image affects the precision of line features. Thirdly, the 12-free-parameter intrinsic matrix proposed by Dansereau *et al.* [6] is redundant and dependent which makes it hard to represent the projection except points.

In this paper, a novel light field camera calibration method is proposed. Compared with point and line, conic has two advantages: one is that conic is well studied in mathematics and can be simply represented by a 3×3 matrix, the other is that conics can be detected and estimated robustly by existing algorithms. Although conic pattern has been used to calibrate traditional camera over decades, few attentions are drawn to light field camera calibration. In addition, several tradition camera calibration methods only consider the estimation of intrinsic parameters without distortion model and optimization, which is not appropriate for light field camera. The extrinsic parameters and distortion model are necessary for distortion rectification and 3D reconstruction. Consequently, instead of using the checkerboard, we creatively design a concentric conics pattern with known size (*i.e.* a circle and a ellipse with the same center) for light field camera calibration. We first exploit the property and reconstruction of self-polar triangle which is shared by concentric circle and ellipse. In addition, with the introduction of light field projection model, an effective linear initial solution for both intrinsic and extrinsic parameters is computed, making use of the property of common self-polar triangle. Furthermore, considering the effect of shifted view, a 4-parameter radial distortion model is defined. We present an effective Sampson cost function for optimization. Finally, we illustrate empirical performances in calibrating synthetic light field camera as well as commercial Illum light field cameras [20]. Quantitative and qualitative analyses verify the effectiveness and robustness of the proposed method.

Our main contributions are:

(1) The property of self-polar triangle which is common to concentric circle and ellipse is explored.
(2) A creative conics pattern which includes circles and ellipses is designed for light field camera calibration.
(3) An effective intrinsic and extrinsic calibration algorithm is proposed, including a linear initial solution, a 4-parameter radial distortion model for light field camera and a novel Sampson cost function for optimization.

2 Related Work

Light Field Calibration. Many research groups [2,3,6,15,29,30,34,35] have explored various light field camera calibration methods making use of the checkerboard or dot grid pattern in decades, where multiple viewpoints or micro-lens images are easy to be synthesized to describe the ray. A plane and parallax framework [30] is proposed to calibrate the camera array system. Johannsen *et al.* [15] exhibit metric calibration and depth distortion for the focused light

field camera [25] through a dot grid pattern with know size. In addition, Thomason *et al.* [29] focus on geometrical distribution of micro-lens array and estimated its position and orientation.

Recently, Dansereau *et al.* [6] propose a light field camera model from a conventional pinhole lenslet and thin-lens model to calibrate light field camera through checkerboard pattern. They derive a 12-free-parameter intrinsic matrix to correspond recorded pixels to light rays in the 3D space (in nonlinear optimization, 10 intrinsic parameters and 5 distortion coefficients are finally estimated). Nevertheless, the calibration method is initialized by a traditional camera calibration algorithm which is not effective to generate all intrinsic parameters. More importantly, since the intrinsic matrix has redundancy and dependency, the decoded rays transformed through intrinsic matrix do not keep regular sampling. Differing from the calibration based on sub-aperture images, Bok *et al.* propose to directly extract line feature from the raw data for initial estimation of intrinsic parameters [2,3]. However, the detectability of line feature plays a crucial role to calibrate light field camera accurately (in practice, the checkerboard should be shot under an unfocused status in order to make the measurements detectable).

More recently, Zhang *et al.* [34] propose a simplified projective model on the reconstructed scene in the 4D light field. They established light field camera geometry for calibration by a 4-parameter model. In addition, a parallel bi-planar dot grid board is designed to provide prior scene points for calibration. This model just assumes that the image and view planes are Euclidean coordinates having equal scales in both axial directions. Nevertheless, there is additional possibility that light field camera contains non-square pixels. For this reason, unequal scale factors are introduced in each direction to explore the relationship between the pixels recorded by the camera and the decoded rays in the 3D space. Zhang *et al.* [35] propose a multi-projection-center model with 6 intrinsic parameters for light field camera. A 3D projective transformation is deduced to describe the relationship between geometric structure and the light field camera coordinates. Based on the camera model and projective transformation, a light field camera calibration method is proposed to verify the effectiveness of multi-projection-center model.

Conics for Calibration. Conic patterns have been utilized in tradition camera calibration over decades. Quan *et al.* [24] geometrically propose the invariants of two coplanar conics through the common self-polar triangle of two concentric circles. Kim *et al.* [17] explore the projective properties of the feature consisted of two concentric circles. They put algebraic and geometric constraints on the linear combination of two concentric circle images to recover the imaged circle center and circular points respectively. Previous approaches usually recover the center of conic and vanishing line in separate steps.

Recently, Huang *et al.* [12] explore properties of the common self-polar triangle of concentric circles. Making use of these properties, the imaged circle center and vanishing line of support plane can be recovered simultaneously. These properties can also be applied to estimate the intrinsic parameters of traditional cam-

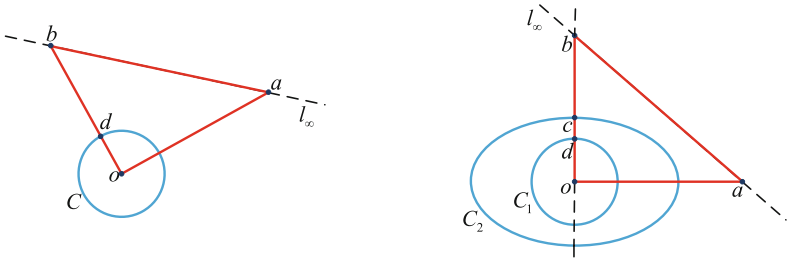

(a) Self-polar triangle (b) Common self-polar triangle

Fig. 1. An illustration of self-polar triangle and common self-polar triangle. $\boldsymbol{o}$ is the center of conics, and $\boldsymbol{l}_\infty$ is the line at infinity. (a) $\triangle\boldsymbol{oab}$ is the self-polar triangle with respect to $\boldsymbol{C}$. (b) $\triangle\boldsymbol{oab}$ is the common self-polar triangle with respect to concentric circle $\boldsymbol{C}_1$ and ellipse $\boldsymbol{C}_2$.

era. In addition, Huang *et al.* [13] investigate the location features of the common self-polar triangle of separate ellipses. Then, a novel approach for homography estimation is proposed. However, these methods only consider the estimation of intrinsic parameters. Little attention has been paid to estimate and optimize extrinsic parameters and lens distortion of light field camera based on concentric conics pattern simultaneously, which are also necessary for camera calibration. In the work, considering that the conic is well studied in mathematics and easy to be represented by matrix, we explore the property of concentric conics for light field camera calibration.

3 Common Self-polar Triangle of Concentric Conics

A point $\boldsymbol{x}$ and conic $\boldsymbol{C}$ define a line $\boldsymbol{l} = \boldsymbol{C}\boldsymbol{x}$ which is described as *pole-polar relationship* [11]. The line $\boldsymbol{l}$ is called the *polar* of $\boldsymbol{x}$ with respect to $\boldsymbol{C}$, and the point $\boldsymbol{x}$ is the *pole* of $\boldsymbol{l}$ with respect to $\boldsymbol{C}$.

Self-polar triangle is defined as, just as Fig. 1(a) shown, the vertices of the triangle are the poles of a conic and their respective polars form its opposite sides [19,28]. A self-polar triangle which is shared by several conics is what we called *common self-polar triangle*, as shown in Fig. 1(b).

Three theorems are illustrated for proving the property of common self-polar triangle.

- The polar line $\boldsymbol{l} = \boldsymbol{C}\boldsymbol{x}$ of the point $\boldsymbol{x}$ with respect to a conic $\boldsymbol{C}$ intersects the conic in two points. The two lines tangent to $\boldsymbol{C}$ at these points intersect at $\boldsymbol{x}$.
- If a point $\boldsymbol{x}$ is on the polar of $\boldsymbol{y}$, then $\boldsymbol{y}$ is on the polar of $\boldsymbol{x}$.
- The circle has infinite self-polar triangles which are right triangles. These triangles share one common vertex and the opposite side of this vertex lies on the same line which are the center of circle and the line at infinity respectively.

3.1 Property of Common Self-polar Triangle

Property 1. The concentric circle and ellipse have and only have one common self-polar triangle which is right triangle. The three sides of this common self-polar triangle are major axis, minor axis and the line at infinity.

Proof. This property is elucidated in Fig. 1(b). Consider the point $\boldsymbol{o}$ denoting the center of concentric circle $\boldsymbol{C}_1$ and ellipse $\boldsymbol{C}_2$. Then, we obtain pole-polar relationships (*i.e.* $\boldsymbol{l}_\infty \sim \boldsymbol{C}_1\boldsymbol{o}$ and $\boldsymbol{l}_\infty \sim \boldsymbol{C}_2\boldsymbol{o}$, where $\sim$ refers to equality up to a scale) [11]. Obviously, $\boldsymbol{o}$ and $\boldsymbol{l}_\infty$ are a common pole-polar which is shared by $\boldsymbol{C}_1$ and $\boldsymbol{C}_2$.

Then, consider a point $\boldsymbol{a}$ on $\boldsymbol{l}_\infty$. The polars of $\boldsymbol{a}$ with respect to $\boldsymbol{C}_1$ and $\boldsymbol{C}_2$ are $\boldsymbol{l}_1$ and $\boldsymbol{l}_2$ respectively which go through the center of concentric conics (*i.e.* $\boldsymbol{l}_1 \sim \boldsymbol{C}_1\boldsymbol{a}$, $\boldsymbol{l}_2 \sim \boldsymbol{C}_2\boldsymbol{a}$). Consider $\boldsymbol{l}_1$ and $\boldsymbol{l}_2$ intersecting with $\boldsymbol{C}_1$ and $\boldsymbol{C}_2$ at points $\boldsymbol{c}$ and $\boldsymbol{d}$ respectively. It is noticed that $\boldsymbol{l}_1$ and $\boldsymbol{l}_2$ intersect at center point $\boldsymbol{o}$. According to the theorem mentioned above, $\triangle\boldsymbol{oab}$ is a self-polar triangle and a right triangle with the assumption that $\boldsymbol{l}_1$ intersects with $\boldsymbol{l}_\infty$ at point $\boldsymbol{b}$.

If $\triangle\boldsymbol{oab}$ is the common self-polar triangle of $\boldsymbol{C}_1$ and $\boldsymbol{C}_2$, then $\boldsymbol{l}_1$ and $\boldsymbol{l}_2$ are common lines which intersect at $\boldsymbol{b}$ on infinite line. According to the theorem of self-polar triangle with respect to circle, we have

$$\boldsymbol{l_{oa}} \perp \boldsymbol{l_{ob}},\ \boldsymbol{l_{ad}} \perp \boldsymbol{l_{ob}},\ \boldsymbol{l_{ad}} \parallel \boldsymbol{l_{ac}} \ \Rightarrow\ \boldsymbol{l_{ac}} \perp \boldsymbol{l_{ob}}. \tag{1}$$

Meanwhile, $\boldsymbol{l_{ac}}$ is also the tangent line of ellipse $\boldsymbol{C}_2$ which is orthogonal to $\boldsymbol{l_{ob}}$. As a result, the line $\boldsymbol{l_{ob}}$ is the major or minor axis of ellipse $\boldsymbol{C}_2$.

If $\boldsymbol{l_{oc}}$ is the major or minor axis of ellipse $\boldsymbol{C}_2$, then we obtain

$$\boldsymbol{l_{ac}} \perp \boldsymbol{l_{oc}},\ \boldsymbol{l_{ad}} \perp \boldsymbol{l_{od}},\ \boldsymbol{l_{ad}} \parallel \boldsymbol{l_{ac}} \ \Rightarrow\ \boldsymbol{l_{oc}} \parallel \boldsymbol{l_{od}}. \tag{2}$$

Due to the same point $\boldsymbol{o}$ which is common to $\boldsymbol{l}_1$ and $\boldsymbol{l}_2$, $\triangle\boldsymbol{oab}$ is the only one common self-polar triangle shared by concentric circle $\boldsymbol{C}_1$ and ellipse $\boldsymbol{C}_2$. □

3.2 Reconstruction of Common Self-polar Triangle

According to the *Property* 1, we find that the common self-polar triangle of concentric circle and ellipse has three special sides which are major axis, minor axis and the line at infinity. In addition, one vertex of this common self-polar triangle lies at the center of concentric circle and ellipse. In this section, we propose a method to reconstruct the only one common self-polar triangle of concentric circle and ellipse. Without loss of generality, the matrix representations of the circle $\boldsymbol{C}_1$ and ellipse $\boldsymbol{C}_2$ are

$$\boldsymbol{C_1} = \begin{bmatrix} 1 & 0 & -x_0 \\ 0 & 1 & -y_0 \\ -x_0 & -y_0 & x_0^2 + y_0^2 - r^2 \end{bmatrix} \quad \text{and} \quad \boldsymbol{C_2} = \begin{bmatrix} \frac{1}{a^2} & 0 & -\frac{x_0}{a^2} \\ 0 & \frac{1}{b^2} & -\frac{y_0}{b^2} \\ -\frac{x_0}{a^2} & -\frac{y_0}{b^2} & \frac{x_0^2}{a^2} + \frac{y_0^2}{b^2} - 1 \end{bmatrix}, \tag{3}$$

where the center of concentric conics is $\boldsymbol{o} = (x_0, y_0)$. The radius of $\boldsymbol{C}_1$ is r, and the major and minor axes of $\boldsymbol{C}_2$ are a and b respectively.

The *Property* 1 substantiates that $\boldsymbol{C}_1$ and $\boldsymbol{C}_2$ only have one common self-polar triangle. In other words, the concentric circle and ellipse have three common pole-polars. What is more, we assume that the point $\boldsymbol{x}$ and line $\boldsymbol{l}$ are satisfied with the pole-polar relationship of $\boldsymbol{C}_1$ and $\boldsymbol{C}_2$ (*i.e.* $\boldsymbol{l} = \boldsymbol{C}_1\boldsymbol{x}$ and $\boldsymbol{l} = \lambda\boldsymbol{C}_2\boldsymbol{x}$, λ is a scale factor). These relationships can be simplified as,

$$\left(\lambda\boldsymbol{I} - \boldsymbol{C}_2^{-1}\boldsymbol{C}_1\right)\boldsymbol{x} = \boldsymbol{0}, \tag{4}$$

where the $\boldsymbol{x}$ is the common pole for $\boldsymbol{C}_1$ and $\boldsymbol{C}_2$. The solutions of Eq. (4) are the eigenvectors of $\boldsymbol{C}_2^{-1}\boldsymbol{C}_1$. We obtain

$$\begin{aligned} \lambda_1 = a^2 &\iff \boldsymbol{e}_1 = (1,0,0)^\top, \\ \lambda_2 = b^2 &\iff \boldsymbol{e}_2 = (0,1,0)^\top, \\ \lambda_3 = r^2 &\iff \boldsymbol{e}_3 = (x_0,y_0,1)^\top, \end{aligned} \tag{5}$$

where λ_1, λ_2 and λ_3 are three different eigenvalues of $\boldsymbol{C}_2^{-1}\boldsymbol{C}_1$ and $\boldsymbol{e}_1$, $\boldsymbol{e}_2$ and $\boldsymbol{e}_3$ are their corresponding eigenvectors. From Eq. (5), the only one common self-polar triangle of concentric circle and ellipse is reconstructed. The major and minor axes of ellipse are intersected with infinite line at the eigenvectors $\boldsymbol{e}_1$ and $\boldsymbol{e}_2$, which represent the direction of major and minor axes respectively. Due to different λ_1 and λ_2, the corresponding eigenvectors $\boldsymbol{e}_1$ and $\boldsymbol{e}_2$ are easy to distinguish for calculating the camera rotation parameters. What is more, the eigenvector $\boldsymbol{e}_3$ is the center of concentric circle and ellipse.

4 Light Field Camera Calibration

4.1 Light Field Projection Model and Its Coordinates

Light field cameras, especially micro-lens array assembled inside, which are innovated from traditional 2D camera, record the 3D world in different but similar rays. With the shifted view, light field camera maps the 3D world to many sub-aperture images. In general, the ray recorded in the 4D light field is parameterized in a *relative* two-parallel-plane coordinates [18], where $Z = 0$ denotes the view plane and $Z = f$ for the image plane. According to the multi-projection-center model [35] which is proposed to describe light field camera, a 3D point $\boldsymbol{X} = (X, Y, Z)^\top$ is mapped to the pixel (x, y) in the image plane,

$$\lambda \begin{bmatrix} x \\ y \\ 1 \end{bmatrix} = \begin{bmatrix} f & 0 & 0 & -fs \\ 0 & f & 0 & -ft \\ 0 & 0 & 1 & 0 \end{bmatrix} \begin{bmatrix} X \\ Y \\ Z \\ 1 \end{bmatrix}. \tag{6}$$

In addition, consider $\boldsymbol{X}_{\boldsymbol{w}}$ denoting the scene point in the world coordinates, the transformation between world and camera coordinates is described by a rotation $\boldsymbol{R} = (\boldsymbol{r_1}, \boldsymbol{r_2}, \boldsymbol{r_3}) \in SO(3)$ and a translation $\boldsymbol{t} = (t_x, t_y, t_z)^\top \in \mathbb{R}^3$, formulated as $\boldsymbol{X} = \boldsymbol{R}\boldsymbol{X}_{\boldsymbol{w}} + \boldsymbol{t}$.

The ray captured by the camera is expressed as $\boldsymbol{p} = (i, j, u, v)$ in term of pixel dimension, where (i, j) are the *absolute* indices of the view, and (u, v) are

the *relative* pixel indices of sub-aperture image at the view (i, j). The light field $L(i, j, u, v)$ recorded by the camera is transformed into a normalized (*i.e.*, the spacing f between two planes is set to unit length for simplicity) undistorted physical light field $L(s, t, x, y)$ by a homogeneous decoding matrix $\boldsymbol{D} \in \mathbb{R}^{5\times5}$ [35],

$$\begin{bmatrix} s \\ t \\ x \\ y \\ 1 \end{bmatrix} = \underbrace{\begin{bmatrix} k_i & 0 & 0 & 0 & 0 \\ 0 & k_j & 0 & 0 & 0 \\ 0 & 0 & k_u & 0 & u_0 \\ 0 & 0 & 0 & k_v & v_0 \\ 0 & 0 & 0 & 0 & 1 \end{bmatrix}}_{=:\boldsymbol{D}} \begin{bmatrix} i \\ j \\ u \\ v \\ 1 \end{bmatrix} = \begin{bmatrix} \boldsymbol{K}_{ij} & \boldsymbol{O}_{2\times3} \\ \boldsymbol{O}_{3\times2} & \boldsymbol{K}_{uv} \end{bmatrix} \begin{bmatrix} i \\ j \\ u \\ v \\ 1 \end{bmatrix}, \tag{7}$$

where $(k_i, k_j, k_u, k_v, u_0, v_0)$ are intrinsic parameters of a light field camera. (k_i, k_j) are scale factors for s and t axes in the view plane and (k_u, k_v) for x and y axes in the image plane respectively. $(-u_0/k_u, -v_0/k_v)$ represent the coordinates of principal point in the sub-aperture image.

4.2 Initialization

The relationship between sub-aperture image pixel (u, v) and 3D world point $\boldsymbol{X}_w$ is extended by Eqs. (6), (7) and extrinsic parameters $[\boldsymbol{R}|\boldsymbol{t}]$,

$$(u, v, 1)^\top \sim \underbrace{\boldsymbol{K}_{uv}^{-1}\,[\boldsymbol{r}_1, \boldsymbol{r}_2, \boldsymbol{r}_3, \boldsymbol{t} - \boldsymbol{t}_{st}]}_{=:\boldsymbol{P}(s,t)} (X_w, Y_w, Z_w, 1)^\top, \tag{8}$$

where $\sim$ refers to the equality up to a scale, $\boldsymbol{t}_{st} = (s, t, 0)^\top$ and $(s, t)^\top = \boldsymbol{K}_{ij}(i, j)^\top$. Moreover, the projection between the plane at infinity and sub-aperture image can be described by planar homography $\boldsymbol{H}_\infty = \boldsymbol{K}_{uv}^{-1}\boldsymbol{R}$. Note that this projection is independent to the shifted view and the position of light field camera. Since the absolute conic $\boldsymbol{\Omega}_\infty$ is on the plane at infinity [11], the sub-aperture image of absolute conic in light field can be described by the conic $\boldsymbol{\omega} = \boldsymbol{K}_{uv}^{-\top}\boldsymbol{K}_{uv}$. More importantly, $\boldsymbol{u}_a^\top\boldsymbol{\omega}\boldsymbol{u}_b = 0$ only if the image points $\boldsymbol{u}_a$ and $\boldsymbol{u}_b$ correspond to the orthogonal directions.

Without loss of generality, we assume the conic pattern is on the plane $Z_w = 0$ in the world coordinates. Consequently, Eq. (8) is simplified as,

$$(u, v, 1)^\top \sim \underbrace{\boldsymbol{K}_{uv}^{-1}\,[\boldsymbol{r}_1, \boldsymbol{r}_2, \boldsymbol{t} - \boldsymbol{t}_{st}]}_{=:\boldsymbol{H}_{ij}} (X_w, Y_w, 1)^\top, \tag{9}$$

where $\boldsymbol{H}_{ij}$ is the planar homography. Supposing $\widetilde{\boldsymbol{C}}_1$ and $\widetilde{\boldsymbol{C}}_2$ represent the projections of concentric circle and ellipse in the sub-aperture image of the view (i, j), we have

$$\widetilde{\boldsymbol{C}}_1 \sim \boldsymbol{H}_{ij}^{-\top}\boldsymbol{C}_1\boldsymbol{H}_{ij}^{-1} \quad \text{and} \quad \widetilde{\boldsymbol{C}}_2 \sim \boldsymbol{H}_{ij}^{-\top}\boldsymbol{C}_2\boldsymbol{H}_{ij}^{-1}, \tag{10}$$

where $\boldsymbol{C}_1$ and $\boldsymbol{C}_2$ are described as Eq. (3) in the world coordinates respectively. Computing the product $\widetilde{\boldsymbol{C}}_2^{-1}\widetilde{\boldsymbol{C}}_1$, we obtain

$$\widetilde{\boldsymbol{C}}_2^{-1}\widetilde{\boldsymbol{C}}_1 \sim \left(\boldsymbol{H}_{ij}^{-\top}\boldsymbol{C}_2\boldsymbol{H}_{ij}^{-1}\right)^{-1}\left(\boldsymbol{H}_{ij}^{-\top}\boldsymbol{C}_1\boldsymbol{H}_{ij}^{-1}\right) = \boldsymbol{H}_{ij}\left(\boldsymbol{C}_2^{-1}\boldsymbol{C}_1\right)\boldsymbol{H}_{ij}^{-1}. \tag{11}$$

As illustrated in Eqs. (5) and (11), $\widetilde{\boldsymbol{C}}_2^{-1}\widetilde{\boldsymbol{C}}_1$ is the similar matrix of $\boldsymbol{C}_2^{-1}\boldsymbol{C}_1$, which means they have the same eigenvalues (*i.e.*, λ_1, λ_2 and λ_3). In addition, the corresponding eigenvectors can be projected by $\boldsymbol{H}_{ij}$ (*i.e.*, $\boldsymbol{e}_k^{(i,j)} \sim \boldsymbol{H}_{ij}\boldsymbol{e}_k$, $k = 1, 2, 3$). According to the *Property* 1 and Eq. (5), the only common self-polar triangle of sub-aperture image is reconstructed. Furthermore, the vanishing lines and center of concentric ellipse are recovered for light field camera calibration. More importantly, the major and minor axes (*i.e.*, $\boldsymbol{e}_1^{(i,j)}$ and $\boldsymbol{e}_2^{(i,j)}$) of ellipse in the sub-aperture image of the view (i, j) imply the rotation of light field camera. Due to different eigenvalues λ_1 and λ_2, the corresponding eigenvectors $\boldsymbol{e}_1^{(i,j)}$ and $\boldsymbol{e}_2^{(i,j)}$ are easy to distinguish for calculating $\boldsymbol{r}_1$ and $\boldsymbol{r}_2$ respectively.

Based on the theorem that there are infinite right self-polar triangles with respect to the circle, two self-polar triangles of the circle are randomly formed to generate the conjugate pairs with respect to $\boldsymbol{\omega}$,

$$\boldsymbol{u}_a^\top \boldsymbol{\omega} \boldsymbol{u}_b = 0 \iff \boldsymbol{u}_a^\top \boldsymbol{K}_{uv}^\top \boldsymbol{K}_{uv} \boldsymbol{u}_b = 0, \tag{12}$$

where $\boldsymbol{u}_a$ and $\boldsymbol{u}_b$ are the points on the vanishing line. In addition, $\boldsymbol{u}_a$ and $\boldsymbol{u}_b$ represent the direction of two cathetuses with respect to self-polar triangle. Once $\boldsymbol{\omega}$ is computed, it is easy to estimate $\boldsymbol{K}_{uv}$ to obtain intrinsic parameters except k_i and k_j by Cholesky factorization [10]. Besides, the rest intrinsic parameters and extrinsic parameters of different poses can be obtained as follows,

$$\tau = \sqrt{\frac{1}{2}\left(\frac{r^2}{|\lambda_{\widehat{C}_1}|} + \frac{b^2}{|\lambda_{\widehat{C}_2}|}\right)}, \quad \widehat{\boldsymbol{C}}_1 = \frac{\hat{\boldsymbol{K}}_{uv}^{-1}\widetilde{\boldsymbol{C}}_1\hat{\boldsymbol{K}}_{uv}}{\|\hat{\boldsymbol{K}}_{uv}^{-1}\widetilde{\boldsymbol{C}}_1\hat{\boldsymbol{K}}_{uv}\|}, \quad \widehat{\boldsymbol{C}}_2 = \frac{\hat{\boldsymbol{K}}_{uv}^{-1}\widetilde{\boldsymbol{C}}_2\hat{\boldsymbol{K}}_{uv}}{\|\hat{\boldsymbol{K}}_{uv}^{-1}\widetilde{\boldsymbol{C}}_2\hat{\boldsymbol{K}}_{uv}\|}, \tag{13}$$

$$\left[\begin{array}{ccc:cc} \boldsymbol{I}_{3\times3} & \boldsymbol{O}_{3\times3} & \boldsymbol{O}_{3\times5} & & \\ \boldsymbol{O}_{3\times3} & \boldsymbol{I}_{3\times3} & \boldsymbol{O}_{3\times5} & & \\ & & & -i & 0 \\ x_0\boldsymbol{I}_{3\times3} & y_0\boldsymbol{I}_{3\times3} & \boldsymbol{I}_{3\times3} & 0 & -j \\ & & & 0 & 0 \end{array}\right] \left[\begin{array}{c} \boldsymbol{r}_1 \\ \boldsymbol{r}_2 \\ \boldsymbol{t} \\ k_i \\ k_j \end{array}\right] = \left[\begin{array}{c} \dfrac{\hat{\boldsymbol{K}}_{uv}\boldsymbol{e}_1^{(i,j)}}{\|\hat{\boldsymbol{K}}_{uv}\boldsymbol{e}_1^{(i,j)}\|} \\ \dfrac{\hat{\boldsymbol{K}}_{uv}\boldsymbol{e}_2^{(i,j)}}{\|\hat{\boldsymbol{K}}_{uv}\boldsymbol{e}_2^{(i,j)}\|} \\ \tau\dfrac{\hat{\boldsymbol{K}}_{uv}\boldsymbol{e}_3^{(i,j)}}{\|\hat{\boldsymbol{K}}_{uv}\boldsymbol{e}_3^{(i,j)}\|} \end{array}\right], \tag{14}$$

$$\boldsymbol{r}_3 = \boldsymbol{r}_1 \times \boldsymbol{r}_2, \tag{15}$$

where $\|\cdot\|$ denotes L_2 norm. $\hat{\boldsymbol{K}}_{uv}$ is derived by intrinsic parameters in Eq. (12). $\lambda_{\widehat{C}_1}$ and $\lambda_{\widehat{C}_2}$ are the smallest eigenvalues of $\widehat{\boldsymbol{C}}_1$ and $\widehat{\boldsymbol{C}}_2$ respectively. τ describes the scale factor. (x_0, y_0) is the center of concentric conics in the world coordinates. $\boldsymbol{e}_1^{(i,j)}$, $\boldsymbol{e}_2^{(i,j)}$ and $\boldsymbol{e}_3^{(i,j)}$ are the eigenvectors of $\widetilde{\boldsymbol{C}}_2^{-1}\widetilde{\boldsymbol{C}}_1$ on the view (i, j) corresponding to $\boldsymbol{e}_1$, $\boldsymbol{e}_2$ and $\boldsymbol{e}_3$ depending on different eigenvalues (in Eq. (5)).

4.3 Distortion Model

In light field camera, there exists radial distortion on the image plane and sampling distortion on the view plane because of special sampling design of two-parallel-plane. In this paper, owing to the assumption that angular sampling is

ideal without distortion, we only consider radial distortion on the image plane. The distorted $(\widetilde{x}, \widetilde{y})$ are rectified by the undistorted (x, y) under the view (s, t),

$$\begin{cases} \widetilde{x} = (1 + k_1 r_{xy}^2 + k_2 r_{xy}^4)x + k_3 s \\ \widetilde{y} = (1 + k_1 r_{xy}^2 + k_2 r_{xy}^4)y + k_4 t \end{cases}, \tag{16}$$

where $r_{xy}^2 = x^2 + y^2$ and the undistorted (x, y) are the projected points from the calibration pattern by intrinsic parameters (k_i, k_j) and extrinsic parameters according to Eq. (6). k_1 and k_2 regulate conventional radial distortion in light field camera. Compared with existing radial distortion of light field camera, k_3 and k_4 are added to represent the distortion affected by the shifted view. In summary, we utilize $\boldsymbol{k}^d = (k_1, k_2, k_3, k_4)$ to denote distortion vector.

4.4 Non-linear Optimization

The initial solution computed by the linear method is refined via non-linear optimization. We define a cost function based on Sampson error [11] to acquire the non-linear solution,

$$\sum_{p=1}^{\#pose} \sum_{n=1}^{\#conic} \sum_{i=1}^{\#view} \frac{\left| \widetilde{\boldsymbol{u}}_i^\top \left(\mathcal{P}, \boldsymbol{k}^d, \boldsymbol{R}_p, \boldsymbol{t}_p, \boldsymbol{C}_{w,n} \right) \boldsymbol{C}_i \widetilde{\boldsymbol{u}}_i \left(\mathcal{P}, \boldsymbol{k}^d, \boldsymbol{R}_p, \boldsymbol{t}_p, \boldsymbol{C}_{w,n} \right) \right|}{2 \| \left(\boldsymbol{C}_i \widetilde{\boldsymbol{u}}_i \left(\mathcal{P}, \boldsymbol{k}^d, \boldsymbol{R}_p, \boldsymbol{t}_p, \boldsymbol{C}_{w,n} \right) \right\|}, \tag{17}$$

where $\widetilde{\boldsymbol{u}}$ is the projection of point on $\boldsymbol{C}_{w,n}$ according to Eqs. (6) and (7), followed by the distortion according to Eq. (16). $\boldsymbol{C}_{w,n}$ describes the conics in the world coordinates as Eq. (3). $\mathcal{P}$ and $\boldsymbol{k}^d$ represent intrinsic parameters and distortion vector respectively. Moreover, $\boldsymbol{R}_p$, $\boldsymbol{t}_p$ are extrinsic parameters at each position, where $\boldsymbol{R}_p$ is parameterized by Rodrigues formula [8]. In addition, the Jacobian matrix of cost function is simple and sparse. This non-linear cost function can be solved using Levenberg-Marquardt algorithm based on trust region method [21]. Matlab's lsqnonlin is utilized to carry out the non-linear optimization. The calibration algorithm of light field camera is summarized in Algorithm 1.

5 Experiments

5.1 Simulated Data

In order to evaluate the performance of the proposed method, we simulate a light field camera, whose intrinsic parameters are referred to Eq. (7) (*i.e.* $k_i = 1.4e{-}4$, $k_j = 1.5e{-}4$, $k_u = 2.0e{-}3$, $k_v = 1.9e{-}3$, $u_0 = -0.59$, $v_0 = -0.52$). These parameters are close to the setting of an Illum camera so that we obtain plausible input close to real-world scenario. Three types of calibration patterns are illustrated in Fig. 2.

Performance w.r.t. the Noise Level. In this experiment, we employ the measurements of 3 poses and 7×7 views to demonstrate the robustness of calibration algorithm with three types of calibration patterns. The rotation angles

Algorithm 1. Light Field Camera Calibration Algorithm.

Input: Concentric conics $\boldsymbol{C}_1$ and $\boldsymbol{C}_2$ and projected conics $\widetilde{\boldsymbol{C}}_1$ and $\widetilde{\boldsymbol{C}}_2$ in each view.
Output: Intrinsic parameters $\mathcal{P} = (k_i, k_j, k_u, k_v, u_0, v_0)$;
Extrinsic parameters $\mathbf{R}_p$, $\mathbf{t}_p (1 \leq p \leq P)$;
Distortion vector $\mathbf{d} = (k_1, k_2, k_3, k_4)^\top$.

for $p = 1$ to P **do**
  for each view (i, j) **do**
    Obtain the eigenvectors $(e_1^{(i,j)}, e_2^{(i,j)}, e_3^{(i,j)})$ of $\widetilde{\boldsymbol{C}}_2^{-1}\widetilde{\boldsymbol{C}}_1$. ▷ Eq. (11)
  end for
end for
Obtain four intrinsic parameters (k_u, k_v, u_0, v_0) by Cholesky factorization ▷ Eq. (12)
for $p = 1$ to P **do**
  Get extrinsic parameters $\mathbf{R}_p$ and $\mathbf{t}_p$ ▷ Eqs. (13-15)
end for
Obtain other two intrinsic parameters (k_i, k_j) ▷ Eqs. (13,14)
Initialize distortion coefficient $\mathbf{d} = (0, 0, 0, 0)^\top$
Create the cost function according to intrinsic parameters, extrinsic parameters and distortion coefficient ▷ Eq. (17)
Obtain optimized results using nonlinear LM algorithm

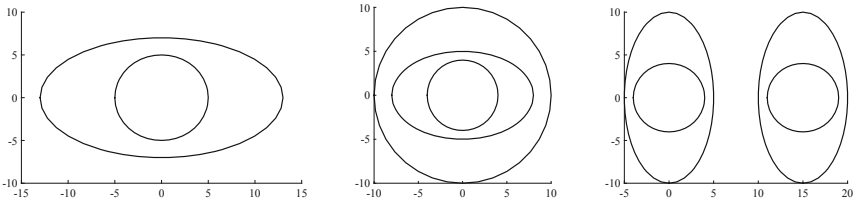

Fig. 2. Three types of calibration patterns evaluated in experiments (unit: *cm*). (a) Two concentric conics. The major and minor axes of ellipse are 13 cm and 7 cm. The radius of circle is 5 cm. (b) Three concentric conics. The radiuses of big circle and small circle are 10 cm and 4 cm respectively. The major and minor axes of ellipse are 8 cm and 5 cm. (c) Two sets of concentric conics. The major and minor axes of ellipse are 8 cm and 5 cm. The radius of circle is 4 cm. The concentric center of right set is $(15, 0)$.

of 3 poses are $(-21°, -14°, 6°)$, $(9°, 5°, 12°)$ and $(-12°, 11°, -4°)$ respectively. We choose 100 points on each conic image to fit the conics, which are projected from the calibration pattern by Eq. (6). Gaussian noise with zero mean and σ standard deviation is added to these points. We vary σ from 0.1 to 1.5 pixels with a 0.1 pixel step. For each noise level, 150 independent trials are conducted. The accuracy is evaluated by the average of relative errors with ground truth. As illustrated in Fig. 3, the errors almost linearly increase with noise level. When the level of noise is fixed, the relative errors are decreased with the number of conics. For the noise level $\sigma = 0.5$, which is larger than normal noise in practical

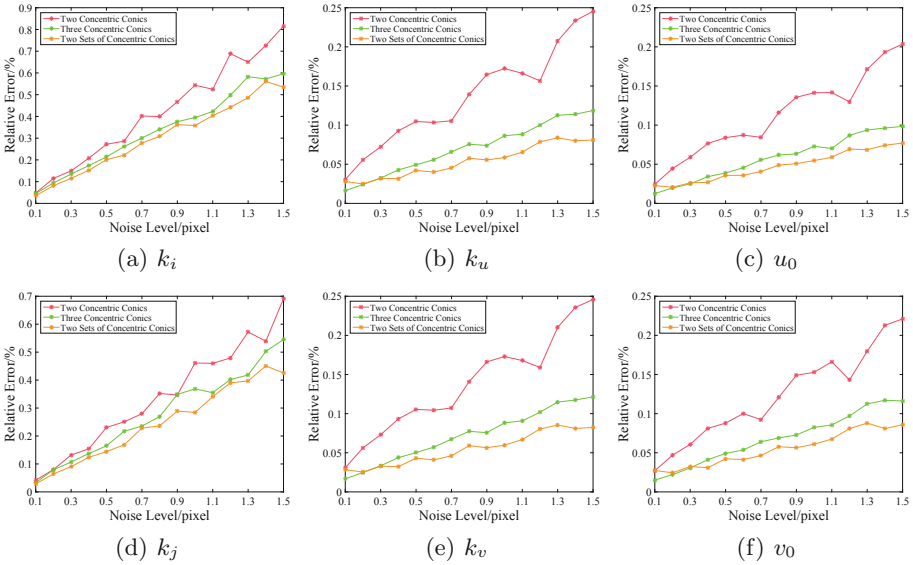

Fig. 3. Performance evaluation of intrinsic parameters on the simulated data with different levels of noise σ.

calibration, the errors of (k_i, k_j) and (k_u, k_v, u_0, v_0) are less than 0.28% and 0.1% respectively, which verifies the robustness of the proposed calibration method to high noise level.

Performance w.r.t. the Number of Poses and Views. In this experiment, we explore the performance with respect to the number of poses and views based on the calibration pattern in Fig. 2(a). We also choose 100 points on each conic. We vary the number of poses from 2 to 8 and the number of views from 3×3 to 7×7. For each combination of pose and view, 100 trails with independent poses are performed by adding the Gaussian noise with zero mean and a standard deviation of 0.5 pixel. The rotation angles are randomly generated from $-30°$ to $30°$. The average relative errors of calibration results with increasing measurements are shown in Fig. 4. The relative errors decrease with the number of views once the number of poses is fixed. Furthermore, the errors reduce with the number of poses. Especially, when $\#pose \geq 4$ and $\#view \geq 5 \times 5$, all relative errors are less than 0.5%, which further exhibits the effectiveness of the proposed method.

5.2 Real Data

The experimental data on real scene light fields are captured by Illum cameras. Two calibration patterns with different configurations and the number of conics are utilized, including a calibration pattern of two concentric conics (seeing Fig. 2(a)) for Illum-1 and Illum-2 and a calibration pattern of three concentric conics (seeing Fig. 2(b)) for Illum-3 and Illum-4. The configurations of two

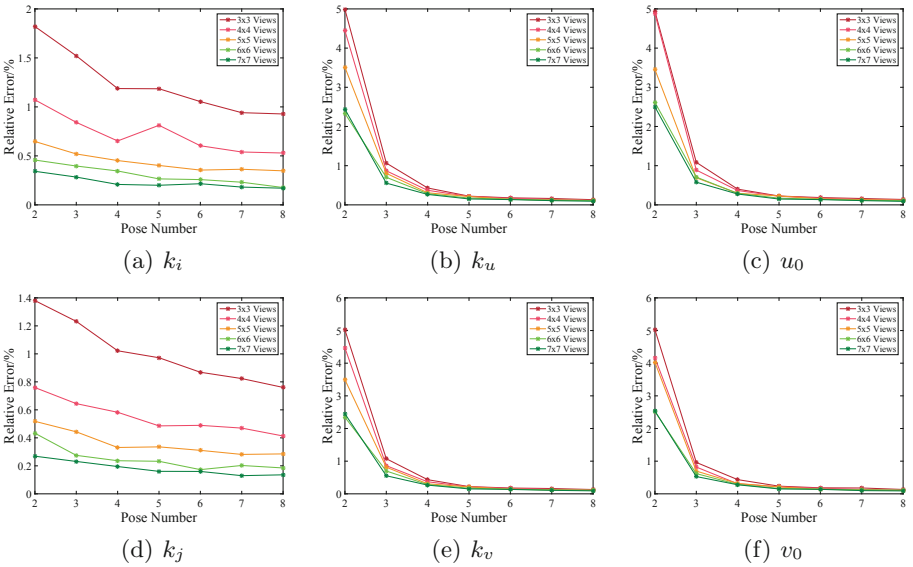

(a) k_i (b) k_u (c) u_0

(d) k_j (e) k_v (f) v_0

Fig. 4. Performance evaluation of intrinsic parameters on the simulated data with different numbers of poses and views.

patterns are also shown in Fig. 2. In the collected datasets, the range does not exceed 60 cm. A white image which is provided by camera is required for locating lenslet image centers and correcting vignetting. After the necessary preprocessing described in [6] (including demosaicing, aligning of the lenslet images and interpolation), the raw 2D lenslet image of light field camera is decoded to a 4D light field representation (*i.e.*, $L(i, j, u, v)$).

The Canny edge detector [4] is utilized to detect the conic from sub-aperture image on the view (i, j). Although the conics appear in all sub-aperture images, the middle 11×11 views are used (15×15 views in total) to produce accurate results. Table 1 summarizes the root mean square (RMS) Sampson errors, as described in Eq. (17), at three calibration stages. Considering the simpleness of conic detection, the proposed method provides an acceptable initial calibration performance. Furthermore, it is more important that the Sampson errors obviously decrease on the item of optimization without distortion, which verifies the effectiveness of cost function. It is noticed that the proposed method achieves smaller Sampson errors once the distortion model is introduced in the optimization. In addition, we compare the proposed method in RMS ray re-projection and re-projection error with state-of-the-art methods, including DPW by Dansereau *et al.* [6] and BJW by Bok *et al.* [3], as illustrated in Table 2. The intersections of major and minor axes with conics and the center of conics are utilized to calculate re-projection error and ray re-projection error. As exhibited in Table 2, the errors of the proposed method are obviously smaller than those of DPW and BJW. Consequently, such optimization results quantitatively substantiate the effectiveness and robustness of light field calibration using conic pattern.

Table 1. RMS Sampson errors of initialization, optimizations without and with distortion (unit: *pixel*). The (N) denotes the number of light fields used for calibration.

	Illum-1 (8)	Illum-2 (10)	Illum-3 (9)	Illum-4 (12)
Initial	5.2401	6.6361	4.1867	5.0426
Opt. w/o distortion	1.1173	1.1081	0.7818	0.7838
Opt. with distortion	0.1746	0.1778	0.2879	0.2889

Table 2. The RMS errors evaluation compared with state-of-the-art methods.

	Re-projection error unit: *pixel*			Ray re-projection error unit: *mm*		
	Ours	DPW [6]	BJW [3]	Ours	DPW [6]	BJW [3]
Illum-1 (8)	**0.3647**	0.5060	0.6084	**0.1692**	0.2736	0.3443
Illum-2 (10)	**0.3805**	0.4902	0.6156	**0.1788**	0.2704	0.3277
Illum-3 (9)	**0.4468**	0.4591	0.6947	**0.2512**	0.3007	0.3963
Illum-4 (12)	**0.4482**	0.4530	0.6780	**0.2471**	0.2988	0.8336

Table 3. Intrinsic parameter estimation results of our datasets.

	Illum-1	Illum-2	Illum-3	Illum-4
k_i	4.6247e−04	4.5028e−04	4.5230e−04	4.4933e−04
k_j	5.9420e−04	5.7428e−04	4.6485e−04	4.7185e−04
k_u	1.0227e−03	1.0541e−03	1.1112e−03	1.1063e−03
k_v	1.0174e−03	1.0493e−03	1.1062e−03	1.1019e−03
u_0	−0.3095	−0.3283	−0.3563	−0.3532
v_0	−0.2282	−0.2318	−0.3511	−0.3478
k_1	−0.3820	−0.3685	−0.1885	−0.1819
k_2	0.5574	0.5915	−0.8067	−0.8885
k_3	1.2206	1.2320	1.4064	1.3972
k_4	1.4654	1.4798	1.4242	1.4296

Table 3 shows the results of intrinsic parameter estimation. The results of Illum-1 and Illum-2 are similar due to the same camera configuration they have. Moreover, the same configuration of Illum-3 and Illum-4 which is different from Illum-1 and Illum-2 leads to similar results of intrinsic parameter estimation. Figure 5 illustrates pose estimation results on our collected datasets.

In order to verify the accuracy of geometric reconstruction of the proposed method compared with baseline methods, we capture a light field of real scene, then reconstruct several typical corner points and estimate the distances

between them as illustrated in Fig. 6. The estimated distances between the reconstructed points are nearly equal to those measured lengths from real objects by rulers (*i.e.* Fig. 6(a)). In addition, Table 4 lists the comparisons of reconstruction results with state-of-the-art methods. The relative errors of reconstruction results demonstrate the performance of our method.

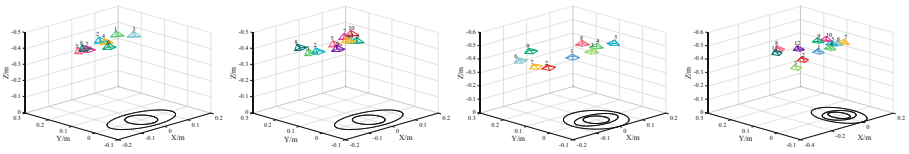

(a) Illum-1 (b) Illum-2 (c) Illum-3 (d) Illum-4

Fig. 5. Pose estimation results of our collected light field datasets.

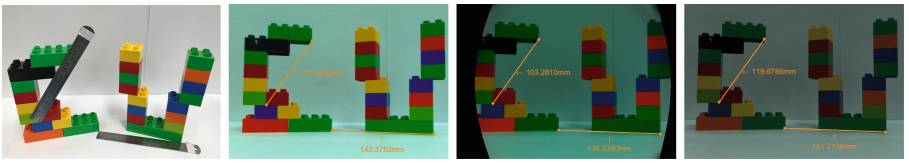

(a) Ruler (b) Ours (c) DPW [20] (d) BJW [24]

Fig. 6. The evaluations of light field measurements. (a) shows distances between 3D points measured by rulers. (b–d) demonstrate the estimated distances using different calibration methods.

Table 4. Quantitative comparison of different calibration methods (unit: *mm*). The relative error is indicated in parentheses.

	Ruler	Ours	DPW [6]	BJW [3]
'C'	117.5000	117.2839 (**0.2**%)	103.2810 (12.2%)	119.6786 (1.9%)
'V'	144.0000	142.3753 (**1.1**%)	136.2380 (5.4%)	141.7118 (1.6%)

6 Conclusion

In the paper, instead of traditional checkerboard, a concentric conics pattern is designed for light field camera calibration. We firstly explore the property

of common self-polar triangle on concentric conics and reconstruct this self-polar triangle. In addition, a light field projection model is utilized to acquire an effective linear initial solution for both intrinsic and extrinsic parameters, making use of the property. Finally, a 4-parameter radial distortion model and a Sampson cost function are defined to non-linearly optimize the 10-parameter model (6 for intrinsic and 4 for distortion). Qualitative and quantitative analyses on extensive experiments verify the effectiveness and robustness of the proposed method. In the future, we intend to concentrate on exploring a unified light field camera calibration method using different types of calibration patterns. The future work also includes conducting different conic detection algorithms to improve the effectiveness of initial solution estimation.

References

1. Birklbauer, C., Bimber, O.: Panorama light-field imaging. In: Computer Graphics Forum, vol. 33, pp. 43–52. Wiley Online Library (2014)
2. Bok, Y., Jeon, H.-G., Kweon, I.S.: Geometric calibration of micro-lens-based light-field cameras using line features. In: Fleet, D., Pajdla, T., Schiele, B., Tuytelaars, T. (eds.) ECCV 2014. LNCS, vol. 8694, pp. 47–61. Springer, Cham (2014). https://doi.org/10.1007/978-3-319-10599-4_4
3. Bok, Y., Jeon, H.G., Kweon, I.S.: Geometric calibration of micro-lens-based light field cameras using line features. IEEE T-PAMI **39**(2), 287–300 (2017)
4. Canny, J.: A computational approach to edge detection. In: Readings in Computer Vision, pp. 184–203. Elsevier (1987)
5. Dansereau, D.G., Mahon, I., Pizarro, O., Williams, S.B.: Plenoptic flow: closed-form visual odometry for light field cameras. In: IEEE IROS, pp. 4455–4462 (2011)
6. Dansereau, D.G., Pizarro, O., Williams, S.B.: Decoding, calibration and rectification for lenselet-based plenoptic cameras. In: IEEE CVPR, pp. 1027–1034 (2013)
7. Dong, F., Ieng, S.H., Savatier, X., Etienne-Cummings, R., Benosman, R.: Plenoptic cameras in real-time robotics. IJRR **32**(2), 206–217 (2013)
8. Faugeras, O.: Three-Dimensional Computer Vision: A Geometric Viewpoint. MIT Press, Cambridge (1993)
9. Guo, X., Yu, Z., Kang, S.B., Lin, H., Yu, J.: Enhancing light fields through ray-space stitching. IEEE T-VCG **22**(7), 1852–1861 (2016)
10. Hartley, R.: Self-calibration of stationary cameras. IJCV **22**(1), 5–23 (1997)
11. Hartley, R., Zisserman, A.: Multiple View Geometry in Computer Vision. Cambridge University Press, Cambridge (2003)
12. Huang, H., Zhang, H., Cheung, Y.M.: The common self-polar triangle of concentric circles and its application to camera calibration. In: IEEE CVPR, pp. 4065–4072 (2015)
13. Huang, H., Zhang, H., Cheung, Y.M.: Homography estimation from the common self-polar triangle of separate ellipses. In: IEEE CVPR, pp. 1737–1744 (2016)
14. Jeon, H.G., et al.: Accurate depth map estimation from a lenslet light field camera. In: IEEE CVPR, pp. 1547–1555 (2015)
15. Johannsen, O., Heinze, C., Goldluecke, B., Perwaß, C.: On the calibration of focused plenoptic cameras. In: Grzegorzek, M., Theobalt, C., Koch, R., Kolb, A. (eds.) Time-of-Flight and Depth Imaging. Sensors, Algorithms, and Applications. LNCS, vol. 8200, pp. 302–317. Springer, Heidelberg (2013). https://doi.org/10.1007/978-3-642-44964-2_15

16. Johannsen, O., Sulc, A., Goldluecke, B.: On linear structure from motion for light field cameras. In: IEEE ICCV, pp. 720–728 (2015)
17. Kim, J.S., Gurdjos, P., Kweon, I.S.: Geometric and algebraic constraints of projected concentric circles and their applications to camera calibration. IEEE T-PAMI **27**(4), 637–642 (2005)
18. Levoy, M., Hanrahan, P.: Light field rendering. In: ACM SIGGRAPH, pp. 31–42 (1996)
19. Liebowitz, D.: Camera calibration and reconstruction of geometry from images. Ph.D. thesis, University of Oxford (2001)
20. Lytro: Lytro redefines photography with light field cameras (2011). http://www.lytro.com
21. Madsen, K., Nielsen, H.B., Tingleff, O.: Methods for Non-linear Least Squares Problems, 2nd edn. Informatics and Mathematical Modelling, Technical University of Denmark, Kongens Lyngby (2004)
22. Ng, R.: Fourier slice photography. ACM TOG **24**(3), 735–744 (2005)
23. Ng, R.: Digital light field photography. Ph.D. thesis, Stanford University (2006)
24. Quan, L., Gros, P., Mohr, R.: Invariants of a pair of conics revisited. In: Mowforth, P. (ed.) BMVC 1991, pp. 71–77. Springer, London (1991). https://doi.org/10.1007/978-1-4471-1921-0_10
25. Raytrix: 3D light field camera technology (2013). http://www.raytrix.de
26. Ren, Z., Zhang, Q., Zhu, H., Wang, Q.: Extending the FOV from disparity and color consistencies in multiview light fields. In: Processing ICIP, pp. 1157–1161 (2017)
27. Si, L., Wang, Q.: Dense depth-map estimation and geometry inference from light fields via global optimization. In: Lai, S.-H., Lepetit, V., Nishino, K., Sato, Y. (eds.) ACCV 2016. LNCS, vol. 10113, pp. 83–98. Springer, Cham (2017). https://doi.org/10.1007/978-3-319-54187-7_6
28. Springer, C.E.: Geometry and Analysis of Projective Spaces, vol. 68. Freeman, New York (1964)
29. Thomason, C., Thurow, B., Fahringer, T.: Calibration of a microlens array for a plenoptic camera. In: AIAA, pp. 1456–1460 (2014)
30. Vaish, V., Wilburn, B., Joshi, N., Levoy, M.: Using plane + parallax for calibrating dense camera arrays. In: IEEE CVPR, pp. 2–9 (2004)
31. Wang, T.C., Efros, A.A., Ramamoorthi, R.: Depth estimation with occlusion modeling using light-field cameras. IEEE T-PAMI **38**(11), 2170–2181 (2016)
32. Wanner, S., Goldluecke, B.: Globally consistent depth labeling of 4D light fields. In: IEEE CVPR, pp. 41–48 (2012)
33. Xiao, Z., Wang, Q., Zhou, G., Yu, J.: Aliasing detection and reduction scheme on angularly undersampled light fields. IEEE TIP **26**(5), 2103–2115 (2017)
34. Zhang, C., Ji, Z., Wang, Q.: Rectifying projective distortion in 4D light field. In: IEEE ICIP (2016)
35. Zhang, Q., Zhang, C., Ling, J., Wang, Q., Yu, J.: A generic multi-projection-center model and calibration method for light field cameras. IEEE T-PAMI (2018). https://doi.org/10.1109/TPAMI.2018.2864617
36. Zhang, Y., Li, Z., Yang, W., Yu, P., Lin, H., Yu, J.: The light field 3D scanner. In: IEEE ICCP, pp. 1–9 (2017)
37. Zhang, Y., Yu, P., Yang, W., Ma, Y., Yu, J.: Ray space features for plenoptic structure-from-motion. In: IEEE ICCV, pp. 4631–4639 (2017)
38. Zhu, H., Wang, Q., Yu, J.: Occlusion-model guided anti-occlusion depth estimation in light field. IEEE J-STSP **11**(7), 965–978 (2017)
39. Zhu, H., Zhang, Q., Wang, Q.: 4D light field superpixel and segmentation. In: IEEE CVPR, pp. 6709–6717 (2017)